Volume 1 | Number 1 | Jan 2013 | Pages 1–100

Journal of
Materials Chemistry A

Materials for energy and sustainability
www.rsc.org/materialsA

Li⁺

ROYAL SOCIETY
OF CHEMISTRY

ROYAL SOCIETY
OF CHEMISTRY

www.rsc.org/materialsA

Journal Name

ARTICLE

Understanding the Effect of Solvent Vapor Annealing on Solution-Processed A-D-A Oligothiophene Bulk-Heterojunction Solar Cells: the Role of Alkyl Side Chains

Cordula D. Wessendorf,*[a] Ana Perez-Rodriguez,[b] Jonas Hanisch,[a] Andreas P. Arndt,[c] Ibrahim Ata,[d] Gisela L. Schulz,[d] Aina Quintilla,[e] Peter Bäuerle,[d] Uli Lemmer,[c,e] Peter Wochner,[f] Erik Ahlswede[a] and Esther Barrena*[b]

Solution-processed bulk heterojunction solar cells consisting of the previously developed dithienopyrrole containing A-D-A oligothiophenes (A = acceptor, D = donor unit) and [6,6]-phenyl-C_{71}-butyric acid methyl ester ($PC_{71}BM$) with power conversion efficiency up to 7.1 % after solvent vapor annealing (SVA) are demonstrated. The influence of the position of the alkyl side chains attached to the thiophene units on the SVA , and the usage of either $PC_{61}BM$ or $PC_{71}BM$ as acceptor, is investigated in more detail by negative secondary ion mass spectrometry (SIMS), Kelvin probe force microscopy (KPFM), photoluminescence (PL), and grazing-incidence X-ray diffraction spectroscopy (GIWAXS). It was found that besides increased crystallinity and domain sizes, the active layers consisting of two different isomers which we will refer to in the following as isomer **1** or isomer **2** (see Fig. 1a) had different compositions after SVA treatment. In the former, a more or less homogeneously-mixed D:A blend was observed, whereas the latter showed a vertical gradient of PCBM in the active layer and much stronger phase segregation on the surface. These findings correlate well with the differences in solar cell performance of both isomers, before and after SVA.

Introduction

Bulk heterojunctions (BHJs), in which electron–donor and electron–acceptor materials are blended together from a common solution, represent the most promising device structure for highly efficient organic solar cells. In the last years huge efforts to increase the efficiencies of BHJ organic solar cells have been made with respect to the development of new absorber materials and device optimization, leading to power conversion efficiencies (PCEs) above 10 % for single,[1-3] 11 % for tandem[4] and 11.8 % for triple[5] structures. These are promising results on the way to highly scalable, low-temperature, cost-efficient solution-based fabrication of organic solar cells.

For optimizing organic solar cells, the control over the structure and spatial organization of D and A materials in the active layer is of enormous importance. Methods for modifying the morphology include for example the use of additives,[6,7] thermal treatment[8] or solvent vapor annealing (SVA).[3,9-12] By choosing structure-defined oligomers as donor materials instead of commonly used polymers, the reproducibility of the solar cells can be increased and the batch-to-batch variations are strongly reduced due to the higher purity of the oligomer compounds.[13,14] Although BJHs solar cells based on small molecules have not been investigated as intensively as polymer solar cells, PCEs close to 10% have also been obtained.[3,12] Further exploration of structure-property relationships in the context of device efficiency will certainly guide to design rules towards better photovoltaic properties and facilitate widespread utilization of solution-processed small molecules. Among a large variety of oligomer donor classes like squaraines,[15] merocyanines[16] and oligothiophenes,[17-20] also co-oligomers consisting of donor and acceptor subunits have also been synthesized.[3,14,21-27]

a. Zentrum für Sonnenenergie- und Wasserstoff-Forschung (ZSW) Baden-Württemberg, Industriestraße 6, 70565 Stuttgart, Germany.
   E-mail: cordula.wessendorf@zsw-bw.de
b. Instituto de Ciencia de Materiales de Barcelona, Consejo Superior de Investigaciones, Cientificas, Campus de la UAB, 08193 Bellaterra, Barcelona, Spain. E-mail: ebarrena@icmab.es
c. Karlsruhe Institute of Technology (KIT), Light Technology Institute, Engesserstraße 13, 76131 Karlsruhe, Germany.
d. University of Ulm, Institute of Organic Chemistry II and Advanced Materials, Albert-Einstein-Allee 11, 89081 Ulm, Germany.
e. Karlsruhe Institute of Technology (KIT), Institute of Microstructure Technology, Hermann-von-Helmholtz-Platz 1, 76344 Eggenstein-Leopoldshafen, Germany.
f. Max Planck Institute for Solid State Research, Heisenbergstraße 1, 70569 Stuttgart, Germany.
†Electronic Supplementary Information (ESI) available: Thickness range against PCE, EQE data, GIWAXS diffraction geometry, AFM topography images, in-plane scans for different angles, additional SIMS analysis. See DOI: 10.1039/x0xx00000x

a)

b)
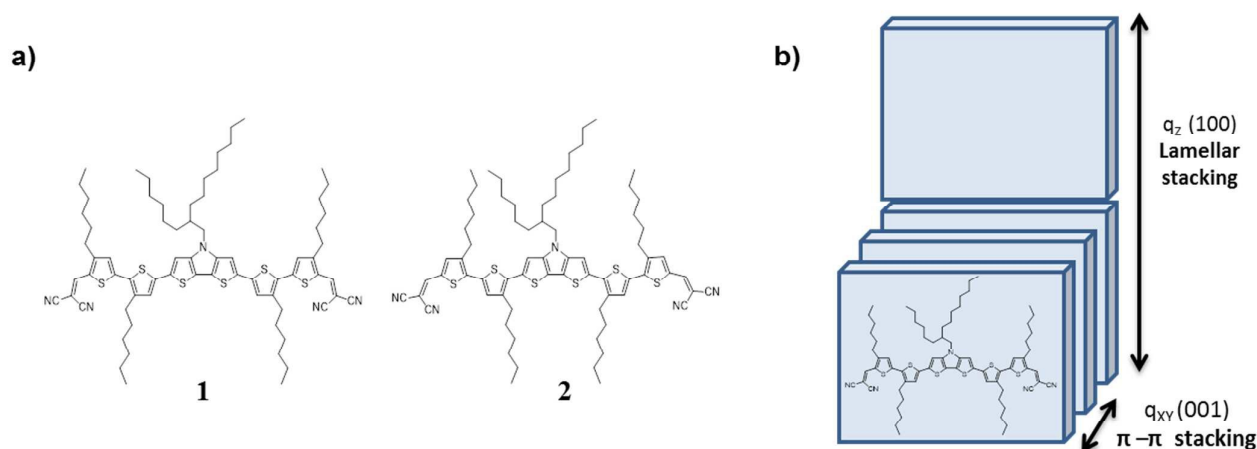
Fig. 1 (a) Chemical structures of A-D-A type oligothiophene **1** and **2**, composed of dicyanovinyl (DCV) groups as terminal acceptor (A) and a fused dithieno[3,2-b:2',3'-*d*]pyrrole (DTP) as a central donor (D) unit, which only differ in the positioning of the side chains; (b) Scheme of molecular packing crystallites with edge-on orientation on the surface.

Recently, we developed and investigated a series of in-air solution-processed A-D-A oligomeric bulk-heterojunction solar cells with a dithienopyrrole (DTP) central unit as donor moiety (D) and dicyanovinyl-substituted oligothiophene acceptor units (A).[28,29] High power conversion PCEs with 5–6 % have been achieved by employing them as donors in BHJ devices with [6,6]-phenyl C_{61}-butyric acid methyl ester (PC$_{61}$BM) as acceptor. The results demonstrate that such a family of A-D-A oligomers holds a large potential for photovoltaics. In the previous work it was shown that both, type and position of the solubilizing alkyl chains affect the solubility of the oligomers and significantly influence the photovoltaic performance of the oligomer:PC$_{61}$BM BHJ devices. The most striking difference between the photovoltaic properties was found for the isomers pair labeled **1** and **2** in the present article (named **3** and **6** in our previous article[29]) (Fig. 1), which differs in the position of the linear alkyl chains, either outer (**1**) or inner (**2**) position. The effectiveness of the SVA turned out to be also very different for both isomers.

The present work aims at gaining an understanding of the structural differences between both isomers in BHJ solar cells that are responsible for their different photovoltaic performances and which can serve as guide in the molecular design and optimization of the devices. In order to get insight into the influence of the SVA treatment, different structural aspects have been investigated, namely, the crystallinity as well as the lateral and vertical phase separated morphology by combining grazing incidence wide angle X-ray scattering (GIWAXS), Kelvin probe force microscopy (KPFM), photoluminescence (PL) and negative secondary ion mass spectrometry (SIMS). For the best performing oligomer (**2**) the study has been extended to the use of PC$_{71}$BM as acceptor, showing that the PCE can be further increased to 7.1% after SVA.

Results and discussion

Photovoltaic and optical properties

As shown in Fig. 1, the only difference between the two structural isomers is the positioning of the regioregular hexyl side chains at either outer (**1**) or inner (**2**) positions of the thiophene rings. The synthesis and characterization was described earlier.[29]

As previously demonstrated, solar cells with **1**:PC$_{61}$BM as absorber material are only slightly improved by SVA with chloroform from 3.8 % to 4.6 % PCE. In contrast, devices based on oligomer **2** show a strong increase in efficiency upon SVA from 1.1 % to 6.1 %.[29]

In the present study we have tested the best performing oligomer **2** with PC$_{71}$BM as acceptor. As PC$_{71}$BM has a much stronger absorbance than PC$_{61}$BM, an increase in efficiency due to higher charge carrier generation rates is expected. Regardless of the use of PC$_{71}$BM or PC$_{61}$BM as electron acceptor, the photovoltaic performance of the blends without SVA is rather low, with similar photovoltaic parameters (Table 1). A drastic improvement is achieved for **2**:PC$_{71}$BM solar cells upon SVA, from 1.1 % PCE to 7.1 % PCE. Fig. 2 displays the corresponding current density–voltage curves of **2**:PC$_{71}$BM solar cells with and without SVA. Clearly, upon SVA both fill factor (FF) and current density (j_{SC}) are strongly improved. This result corresponds well to the findings of Chen and co-workers who tested a series of different solvents for SVA on small molecule solar cells and concluded that good solvents with high vapor pressure lead to the best performances.[12] In contrast the study of Chen,[12] the open circuit voltage (V_{oc}) of our cells is slightly increased upon SVA, but the influence is only marginal and could be related to the differences in the phase segregation of oligomer and fullerene and therewith in recombination effects. As expected, the overall efficiency is higher with PC$_{71}$BM than with PC$_{61}$BM due to increased j_{SC} (12 mA cm^{-2} with PC$_{71}$BM instead of 10 mA cm^{-2} with PC$_{61}$BM) as result of enhanced absorbance. The optimal thickness range for the **2**:PC$_{71}$BM absorber layer was between 90 and 120 nm. (Fig. S1 in the ESI†)

Table 1 Photovoltaic parameters for best and average cells made from oligomers **1** and **2** blended with $PC_{61}BM$ or $PC_{71}BM$, respectively, with and without SVA. The averaged values consist of at least 10 cells.

	SVA (s)	Parameters of best cells				Average	Thickness (nm)
		PCE (%)	V_{OC} (mV)	j_{SC} (mA cm^{-2})	FF (%)	PCE (±std. dev.) (%)	
1:$PC_{61}BM$ (1:2)[a)29]	0	3.8	837	7.1	64	3.1 (±0.33)	
	120	4.6	840	8.4	66	3.5 (±0.51)	62–67
2:$PC_{61}BM$ (1:2)[a)29]	0	1.1	817	4.1	32	0.9 (±0.09)	
	90	6.1	843	10.1	72	5.6 (±0.28)	90–98
2:$PC_{71}BM$ (1:2)[b)]	0	1.1	816	4.4	30	0.8 (±0.18)	
	90	7.1	827	12.0	71	6.9 (±0.11)	114–119

[a)]solution casted at 50°C, [b)]solution casted at room temperature.
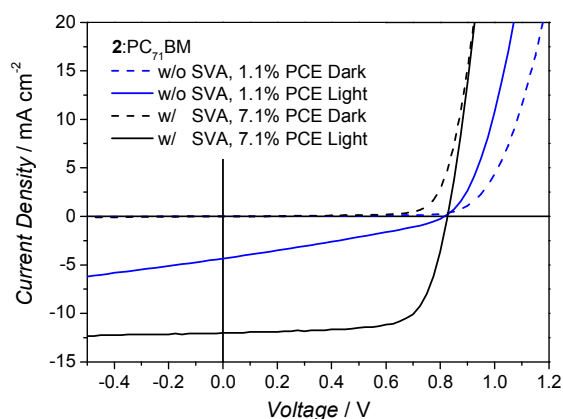
Fig. 2 Current density – voltage curves of **2**:$PC_{71}BM$ solar cells without (blue) and with (black) SVA.

The treatment of SVA leads to strong changes in the UV-visible absorption spectra of the **2**:$PC_{71}BM$ films (Fig. 3). Without SVA (blue) the spectrum has only peaks in the region where the
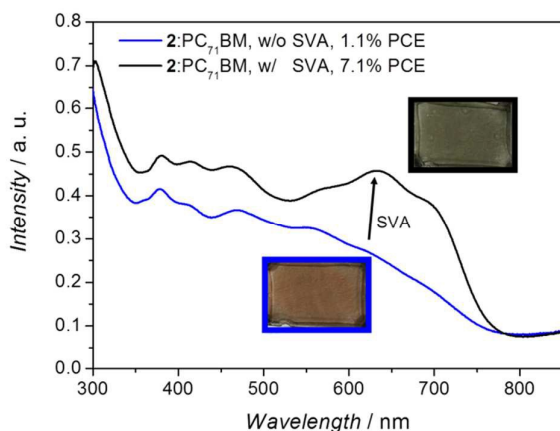
$PC_{71}BM$ absorbs, with a maximum at 378 nm and a shoulder at 410 and at 469 nm. At higher wavelengths the spectrum is relatively featureless in the absorption range of the donor, exhibiting only two broad shoulders around 548 and 617 nm. Similarly, as observed for **2** blended with $PC_{61}BM$,[29] upon SVA the absorption of oligomer **2** is strongly enhanced and exhibits more pronounced spectral features which are strongly red-shifted to 569 (shoulder), 632 (maximum) and 693 (shoulder) nm (black spectrum). The observed changes upon SVA are indicative of significant morphological rearrangements with SVA leading to better molecular packing of the oligomer. These changes are also manifested in a color change of the films from brown without SVA to dark green after SVA (see inserts in Fig. 3).

Fig. 3 Absorption spectra of **2**:$PC_{71}BM$ solar cells without (blue line) and with (black line) SVA. Photographs of the respective layers are shown as inserts to illustrate the change in color. Upon SVA the absorption of the oligomer **2** is strongly enhanced with spectral features shifted to higher wavelengths.

It is seen in Fig. S2 in the ESI† that with SVA **2**:$PC_{71}BM$ solar cells show high (>50%) external quantum efficiency (EQE) across nearly the entire absorption range from 350 to 700 nm with two maxima at 460 and 610 nm. Due to the strong absorption of $PC_{71}BM$ the EQE has a more rectangular shape than with $PC_{61}BM$.[29]
In contrast to compound **2**, with films of **1**:$PC_{71}BM$ no shift of the absorption peaks are obtained after SVA. Only the intensity of the oligomer-correlated maxima is slightly increased as it was also observed for **1**:$PC_{61}BM$ films (ESI† Fig. S3).

Investigation of solvent vapor annealing (SVA) effects on crystallinity and morphology

Extensive studies on polymer BHJs solar cells have revealed that the structure-property relationships are non-trivial and strongly material-dependent. In general, the device performance may be influenced by the donor crystallinity, molecular orientation, extent of the π-π packing and the lateral and vertical nano-to-mesoscale morphologies of these blends.[30]
To develop a deeper understanding of the differences between BHJs with both isomers and the changes induced by SVA, the absorber layers have been investigated by the combination of GIWAXS, PL and KPFM, which provide information about different aspects of the structural properties of the BHJs.
The crystallinity has been primarily probed by grazing incidence wide angle X-ray scattering (GIWAXS). Description and scheme of the diffraction measurement setup are provided in Fig. S4a.
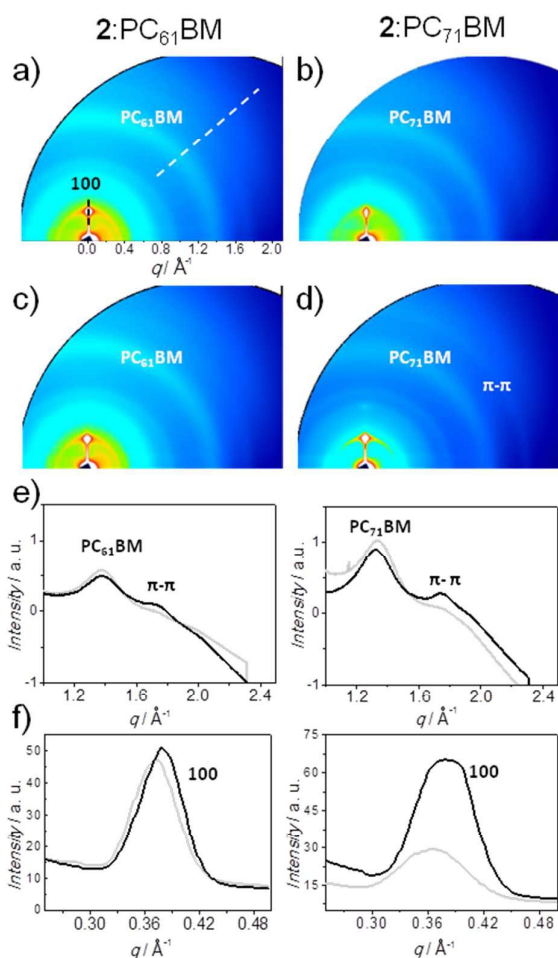
Fig. 4 Two dimensional diffraction patterns of **2**:PC$_{61}$BM and **2**:PC$_{71}$BM (a), (b) before and (c), (d) after 90 s of SVA in chloroform environment. (e) Radial profiles along the marked direction (white dashed line) showing peaks corresponding to PCBM and π-π stacking of the oligomer, and (f) along the (100) Bragg peak (black dashed line) before (grey) and after SVA (black).

The two-dimensional (2D) 2D GIWAXS patterns of neat **1** and **2** films show the (100) Bragg peak corresponding to a lamellar stacking of the oligomers with an average spacing of about 16 Å for **1** and 17 Å for **2** (Table 2 and Fig. S4 in the ESI†). A diffraction ring corresponding to the π-π stacking of the oligomers is also observed with associated spacing of ≈ 3.5 Å. Fig. 4 shows 2D X-ray scattering patterns of **2** in blends either with PC$_{61}$BM (left) or with PC$_{71}$BM (right), before and after 90s of SVA with chloroform. The broad unoriented halo corresponding to the fullerene component is marked in the 2D images. Without SVA, both blends exhibit the (100) diffraction peak of the oligomer and the isotropic scattering ring characteristic of short-range ordered aggregates of the fullerene component (crystalline coherence length of ≈ 3

nm).[31,32] In fact, blending the oligomer with the fullerene derivative does not appreciably change the orientation or spacing of the lamellae (see Fig. S4 and Table 2). The (100) scattering intensity appears as a superposition of a scattering ring that corresponds to the formation of unoriented crystallites and an out-of-plane peak indicating a fraction of crystallites predominantly edge-on oriented (scheme in Fig. 1b) with an angular distribution orientation of ~6º. Such mixture of aligned lamellae and unoriented crystallites has been observed for polymer blends and attributed to heterogeneous nucleation at the film interface and at the bulk of the film.[33] However the faint and almost undistinguishable intensity of the π-π stacking ring indicate that the fullerene impedes to large extent the π-π stacking of the oligomer. The lack of π-π stacking might be related to the larger steric hindrance of the hexyl side chains of the oligomer in solution as measured by UV-vis-absorption.[29] The most remarkable effect of the SVA is the increased intensity of the scattering ring associated with the π-π packing, as can be better observed in the radial scans along the path marked in the reciprocal space maps (Fig. 4e). Note that the scattering intensity associated to the π-π stacking appears as a ring, being therefore associated to the fraction of randomly oriented crystallites in the film. The enhancement of the π-π stacking is consistent with the red-shift and more pronounced features observed in the UV-vis absorption spectrum in Fig. 3 and suggest more extended π-conjugation after SVA. The π-π stacking of oligomers has an important role in facilitating hole mobility and charge delocalization, and therefore it can be one of the factors contributing to the dramatic improvement of photovoltaic performance of the solvent-annealed solar cells based on the oligomer **2**.[34] To estimate the average coherence length of the π-π stacking, in-plane data with a point-detector were collected (Fig. S6 in the ESI†). From the FWHM of the in-plane peak (Δ) a mean coherence length of the π-π stacking of 2π/Δ ~ 10 nm was estimated, which corresponds to ~28 π-π stacked molecules.

A shift of the (100) peak towards larger q values is observed after SVA (Fig. 4f, 5d) indicating a decrease in the average lamella spacing from 17.1 Å to 16.6 Å for **2**:PC$_{71}$BM and from 16.9 to 16.6 Å for **2**:PC$_{61}$BM and therefore a slight densification of the lamella packing. An overview of the (100) q-position of all measured pure oligomers and blends are given in Table 2. Particularly for **2**:PC$_{71}$BM, SVA results in an increased intensity of the (100) Bragg peak indicating an enhancement of the (100) oriented crystallites. Whereas the angular distribution of edge-on oriented crystallites does not significantly change upon SVA, the intensity of the (100) ring does increase for **2**:PC$_{61}$BM and **2**:PC$_{71}$BM, giving evidence for enhanced crystallization of unoriented crystallites.
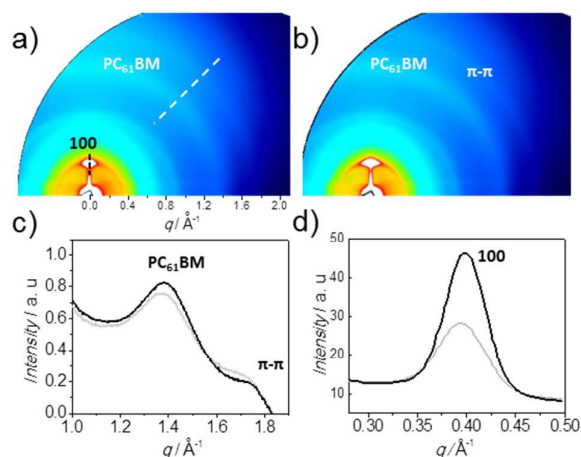
Fig. 5 Two dimensional diffraction pattern of **1**:$PC_{61}BM$ (a) before and (b) after 120 s of SVA in chloroform environment. Radial profiles along marked directions before (grey) and after SVA (black): (c) along white dashed line, showing peaks corresponding to $PC_{61}BM$ and π-π stacking of the oligomer, (d) along black dashed line, the (100) Bragg peak.

Films of **1**:$PC_{61}BM$ exhibit similar structural features as observed with oligomer **2**: a fraction of edge-on oriented oligomer (angular distribution of ≈ 7º) coexisting with randomly oriented crystallites and disordered $PC_{61}BM$. However for the blend **1**:$PC_{61}BM$, the π-π stacking ring is visible even without SVA. The treatment of SVA does not lead to visible changes in the 2D GIWAXS patterns and the radial scan across the PCBM and π-π stacking ring overlaps almost perfectly (Fig. 5a-c). As observed for the oligomer **2**, SVA induces increased intensity of the (100) scattering signal (Fig. 5d), accompanied by a slight decrease of the lamella spacing, in agreement with former findings.[29]

The development of π-π stacking may explain the better power conversion efficiency of solar cells based on the oligomer **1** before SVA. It should be noted that other small-molecules for solar cells such as p-DTS(FBTTh$_2$)$_2$[35] or DRCN7T[36] exhibit GIWAXS patterns with higher-order x-ray reflections indicating a better degree of crystalline order. In contrast, oligomers **1** and **2** show only poor crystallinity but still reasonable efficiencies, indicating that crystalline quality is not a critical factor for this material. The negligible change in the UV-vis

Table 2 Average spacings and Bragg peak positions before and after SVA of either pure oligomers **1** and **2** or blended with $PC_{61}BM$ or $PC_{71}BM$, respectively.

SAMPLE	Average spacing and Bragg peak position			
	Before SVA		After SVA	
	Å	q ($Å^{-1}$)	Å	q ($Å^{-1}$)
1 pure	15.9	0.392		
2 pure	17.0	0.370		
1:$PC_{61}BM$	15.9	0.395	15.8	0.399
2:$PC_{61}BM$	17.0	0.372	16.6	0.378
2:$PC_{71}BM$	17.0	0.367	16.6	0.379

absorption observed for the blends **1**:$PC_{61}BM$[29] despite the observed increase of the intensity of the (100) reflection is also an indication that the crystalline population (associated with the (100) reflection) is not representative of the majority of the film.

We conclude that other factors contribute to the changes in photovoltaic performance and, in particular, to the superior photovoltaic performance of **2**:fullerene solar cells after SVA. It is known that the nano-to-mesoscale morphologies of the blends are also critical for the optimization of the photovoltaic performance.[37-39] To investigate the effect of SVA on the phase segregation within the oligomer-fullerene blends, KPFM imaging turns out to be a capable method enabling insights to the domain formation of the films. KPFM allows measuring the local contact potential between tip and substrate simultaneously with the topography. Thus the spatially resolved surface potential provides information related to local differences in the work function[40, 41] or related to charging phenomena.[42] At the surface of an organic donor-acceptor blend, the sign and magnitude of the measured potential depends on the nature of the underlying substrate.[43] This means that the measured electrostatic potential of donor and acceptor materials depends on charge equilibration with the substrate and on doping or charge transfer between the donor and acceptor. In spite of the multiple factors contributing to the electrostatic potential, KPFM has demonstrated to be a useful tool for the exploration of photo-induced charges of donor:acceptor solar cells at the nanoscale.[44-46]

In the present work, the topographical data show strong increase of the surface roughness upon SVA for **2**:$PC_{61}BM$ films and **2**:$PC_{71}BM$ films, whereas **1**:$PC_{61}BM$ films are only slightly affected by SVA (see Fig. S5). In Fig. 6 KPFM images of all investigated blends are shown with and without SVA. After the solvent vapor treatment a distinct contrast in the surface potential maps becomes apparent for all samples and two different phases can be revealed. We ascribe this observation to re-organization processes during the SVA which leads to a pronounced phase segregation within the oligomer:fullerene derivative blends. In case of **1**:$PC_{61}BM$ blends, the emerging structures in the contact potential difference signal upon SVA show lengths of up to 350 nm whereas for blends composed of oligomer **2** these regions can even be as large as 1 μm. Regarding the high performance of the solar cells, these large domains are more likely to be oligomer and fullerene enriched regions, respectively, rather than pure donor or acceptor phases. Although the spatially resolved contrast in the images cannot directly be assigned to oligomer and fullerene domains, being definitively too large for efficient charge separation in the BHJ, the results suggest, however, larger morphological changes for blends with the oligomer **2**.

The degree of re-organization observed in the blends therefore seems to have a beneficial impact on the formation of charge carrier transport pathways and the overall device performance.
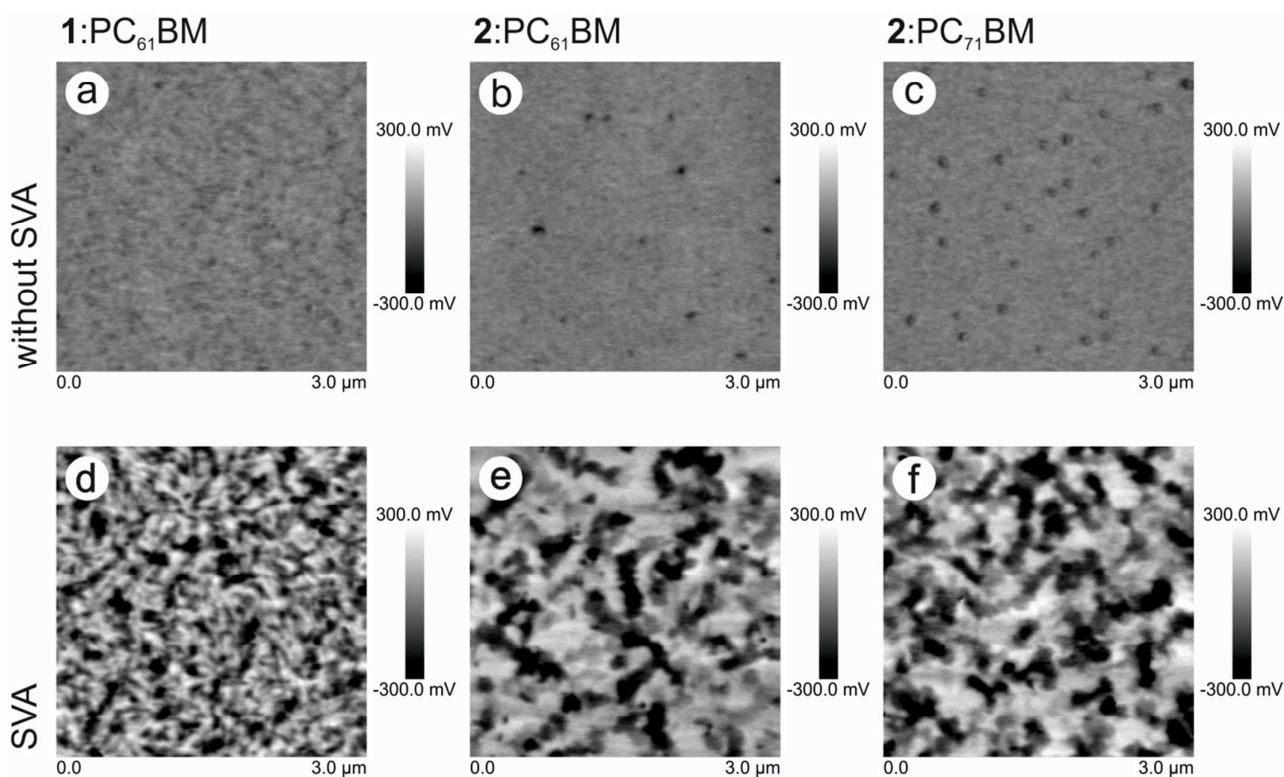
Fig. 6 KPFM images showing the contact potential difference of **1**:PC$_{61}$BM, **2**:PC$_{61}$BM and **2**:PC$_{71}$BM films with and without SVA.

Besides KPFM measurements, also photoluminescence (PL) spectra reveal that the blend morphology changes upon SVA. After SVA for all three blends a significant increase of the PL emission is observed (Fig. 7). The maximum PL intensity rises by a factor of 7.4 for **2**:PC$_{71}$BM and of 6.7 for **2**:PC$_{61}$BM blends while for **1**:PC$_{61}$BM rises only by a factor of 3.2. Variations of film thicknesses between samples with and without SVA are less than 10 %. We therefore can clearly exclude a varying film thickness as cause for the change in PL intensity.

The observed increase of PL is attributed to an increase of the average size of the donor domains within the BHJ upon SVA which enhances the radiative recombination of primarily generated excitons due to their finite lifetime and the increased average distance to a donor-acceptor interface from the initial place of exciton generation. Accordingly, the exciton quenching at the interfaces is reduced for the blends upon SVA which, compared to the improved device performances after the solvent vapor treatment, reveals that the exciton dissociation is not the limiting factor for the lower photocurrent in the **2**:PCBM devices without SVA but rather the charge carrier transport due to its particular morphology.

Thus, PL spectra of BHJs with the oligomer **2** suggest an enhanced re-organization of donor and acceptor molecules upon SVA which is also indicated by the phase segregation on a larger lateral length scale observed by KPFM.
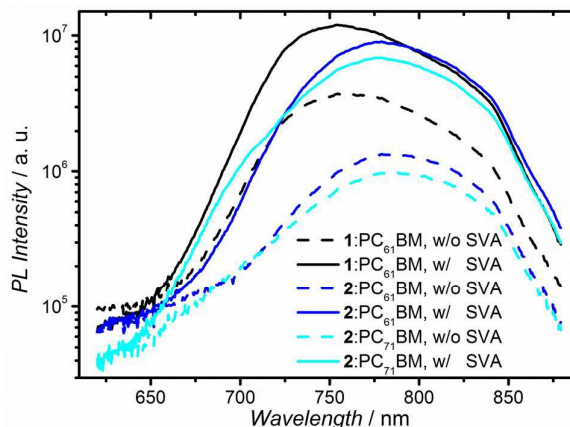
Fig. 7 Photoluminescence spectra of blends containing **1**:PC$_{61}$BM (black), **2**:PC$_{61}$BM (blue) and **2**:PC$_{71}$BM (cyan) without (dash) and with (solid) SVA.

Investigation of the vertical blend composition

To also investigate the influence of the SVA on the vertical phase separation, we have used SIMS depth profiling and angle dependent GIWAXS measurements. Negative SIMS was carried out to have some information about the vertical distribution of the elements in the sample.
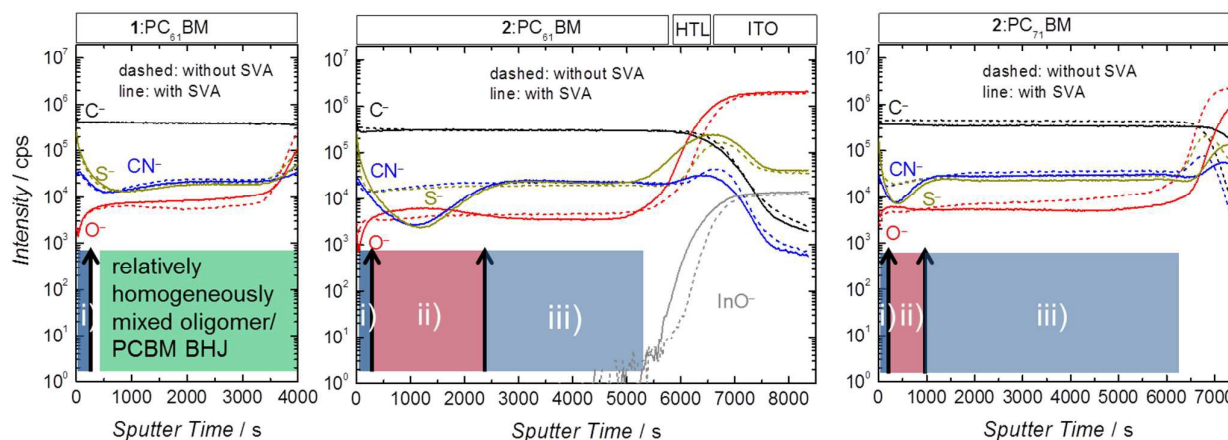
Fig. 8 Negative SIMS depth profiles of **1**:PC$_{61}$BM (left), **2**:PC$_{61}$BM (center) and **2**:PC$_{71}$BM (right) absorber layers on ITO substrates with PEDOT:PSS as hole transport layer (HTL) without (dash) and with (solid) SVA. For the samples with SVA (solid lines) the three regions are marked: i) oligomer-enriched surface, ii) sub-surface region with decreased concentration of oligomer, iii) a slightly oligomer-enriched region up to the bottom interface with more or less constant signals.

Depth profiles of freshly prepared absorber layers of **1**:PC$_{61}$BM (Fig. 8, left), **2**:PC$_{61}$BM (Fig. 8, center) and **2**:PC$_{71}$BM (Fig. 8, right) without (dashed lines) and with SVA (solid lines) on top of PEDOT:PSS and ITO have been examined. The carbon signal (C12$^-$, black) was used for reference, the sulfur (S32$^-$, dark yellow) and cyano group (CN26$^-$, blue) signals are generated exclusively from the oligomer part of the blends, whereas the oxygen (O16$^-$, red) signal derives within the absorber solely from the PCBM. The dramatic rise of the oxygen signal at longer sputter times indicates the position of the interface between PEDOT:PSS layer and ITO substrate, visible also in the InO131$^-$ (grey) signal. The sputter time is consistent with the corresponding different absorber layer thicknesses for a constant sputtering rate of ~0.015 nm/s for the organic layers. Before SVA, the characteristic species used to identify the oligomers (CN26$^-$, S32$^-$) and the fullerene (O16$^-$) are more or less constant as a function of the depth with exception of the air-surface, for which an oligomers-enrichment is observed (first few nanometers) for all the three films. For **1**:PC$_{61}$BM blend (Fig. 8, left), no major changes upon SVA could be detected in the depth profile. This observation is consistent with the slight changes observed in the nanomorphology and structure upon SVA and the little improvement of the solar cells.[29] In contrast, for films with oligomer **2** as donor, drastic changes upon SVA are observed with both, PC$_{61}$BM (center) and PC$_{71}$BM (right), but for PC$_{61}$BM these changes are much more pronounced. In both cases three regions can be distinguished: i) oligomer-enriched surface (upper layer) with low O16$^-$ and with high CN26$^-$ and S32$^-$ signal, ii) sub-surface region with decreased concentration of oligomer, as evidenced by a depletion in the oligomer signals (low CN26$^-$ and S32$^-$ and

increase of the O16$^-$ signal), iii) a slightly oligomer-enriched region up to bottom interface with more or less constant signals.

Hence the results from SIMS reveal that the composition ratio in the vertical direction is also affected by SVA. The ratio of oligomer **2** to PC$_{61}$BM across the film has been calculated from the SIMs depth profiles as it is explained in detail in the ESI† (Fig. S7). The more or less constant ratio in the absorber layer can be seen in the not-solvent-vapor annealed device where after a small oligomer topping layer the ratio of CN26$^-$:O16$^-$ stabilizes at 1:2 (which corresponds to 0.5). In contrast, the calculated ratio of **2**:PC$_{61}$BM for the solvent-vapor-annealed device varies as a function of the depth and shows an oligomer-poor (PCBM-rich) layer (with a very thin oligomer-rich layer on top, with a ratio up to 5:1) close to the air-interface and increased oligomer concentration on the bottom of the film, with a **2**:PC$_{61}$BM mass ratio of nearly 1:1 instead of 1:2 of the absorber solution. This has schematically been drawn in Fig. 10.

Such a vertical gradient is possibly another cause for the dramatic improvement of the solar cells upon SVA. When the anode is enriched with the donor and the cathode with the acceptor, as it is the case with a solvent-vapor-annealed **2**:PC$_{61/71}$BM solar cell, the flow direction of charges is facilitated inside the device and a more efficient extraction of charges is assured. Therefore the series resistance (R_s) is reduced, simultaneously the parallel resistance (R_p) is increased and the j_{SC} is enhanced after SVA of **2**:PC$_{61/71}$BM as it is demonstrated in Fig. 2 and in table S1 in the ESI†.

Interestingly, this vertical gradient is stronger for **2**:PC$_{61}$BM than for **2**:PC$_{71}$BM absorbers. Probably this is because PC$_{71}$BM is a larger molecule than PC$_{61}$BM and therefore less mobile within the absorber blend, however, we do not see that trend in KPFM.

As GIWAXS has only a penetration of a few nm, the upper monolayers of the absorber blends can be studied by angle dependent measurements.

2:PC$_{61}$BM before SVA

2:PC$_{61}$BM after SVA

$\alpha < \alpha_c$ a)

c)

$\alpha > \alpha_c$ b)

d)
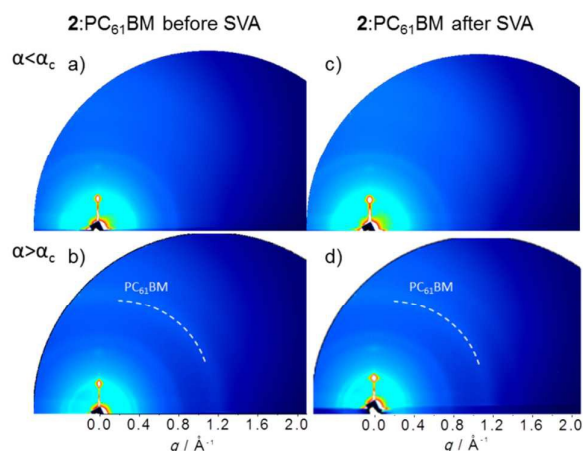
Fig. 9 Two dimensional diffraction patterns of **2**:PC$_{61}$BM before and after solvent annealing, (a) and (c) for incident angle below the critical angle α_c, (b) and (d) for incident angle above α_c.

For **2**:PC$_{61}$BM blends, 2D GIWAXS data were acquired at different incident angles to have depth-resolved information of the structure (Fig. 9 and S6). In the regime of total external reflection, i.e., for incidence angles (α) less than the critical angle (α_c~0.11), a so-called evanescent X-ray wave field forms inside the less dense medium with a penetration depth of only few nm (ca. 7 nm) in the material. In this regime, in the 2D diffraction patterns (Fig. 9a and c), the PCBM ring is not distinguishable while the (100) Bragg peak is clearly visible. For incident angles above the critical angle, i. e. when the x-ray penetrates in the bulk of the film, the PCBM ring appears. These results confirm an oligomer-rich air/film surface that is not affected by the exposure to vapor. The formation of a skin layer on top of the active layer has also been reported for polymer BHJs such as P3HT:PC$_{61}$BM without appreciably impact on the performance of the OPV devices.[47,48]

By combining all findings from SIMS and GIWAXS, we conclude that the absorber layer consists of a few monolayers of oligomer **2** on top, followed by a PCBM-rich / oligomer-poor layer and a slightly oligomer-rich layer at the bottom, as it is depicted in Fig. 10.

oligomer
PCBM
PEDOT:PSS
ITO
Glass

SVA

←i)
←ii)
←iii)

Fig. 10 Scheme of the vertical configuration of the oligomer **2**:PC$_{61\ or\ 71}$BM solar cells. For the solvent-vapor annealed sample three regions are marked: i) oligomer-enriched surface, ii) sub-surface region with decreased concentration of oligomer, iii) a slightly oligomer-enriched region up to the bottom interface.

Discussion

We have shown the important role of the position of the regioregular hexyl side chains of conjugated A-D-A type oligothiophenes, either at outer (**1**) or inner (**2**) positions of the thiophene rings. A previous work reports for oligomer **2** a larger solubility and a blue-shift of the absorption maximum in solution, as compared to oligomer **1**.[29] Both effects seem to be related to steric hindrance between the inner position of the hexyl side chains and the DTP-moiety, causing a twisted backbone of oligomer **2** and enabling a larger interaction between solvent molecules with the hexyl chains. The results from GIWAXS suggest that during the fast drying process, the reduced planarity of the backbone hinders the development of π-π stacking in the as-casted films with oligomer **2**. The outer position of the hexyl chains in oligomer **1** allows higher co-planarity of its molecular backbone, which facilitates the π-π organization of the oligomers during drying. Thus, the improved photovoltaic performance of films with oligomer **1** before SVA can be explained by a higher crystallinity and, plausibly, a better phase-separated nanomorphology. It is remarkable that SVA does not cause major structural changes, in consistence with the little improvement of the solar cells upon SVA, suggesting that blends with oligomer **1** are already in a near equilibrium state after casting.

Structural changes are observed upon SVA for the blends with oligomer **2**. The effect of SVA involves at least two aspects: (i) π-π crystallization of the oligomer (ii) enhanced segregation of the fullerene component. Our SIMS-results suggest that the inner position of the hexyl chains enables higher molecular redistribution when the blends are swollen with solvent molecules as reflected in the formed vertical gradient. The segregation of the fullerene leads to the formation of larger phase-separated domains as revealed by AFM and PL as well as changes in the vertical composition generated by the diffusion of the fullerene to the top of the film as it was confirmed by negative SIMS. After SVA an oligomer-poor layer at the cathode side followed by an oligomer-rich layer at the anode side is obtained. This is beneficial for charge carrier extraction and therefore contributes to a higher current density and improved fill factor of the solvent vapor annealed devices. As the gradient in PCBM content is more dominant for absorbers with **2**:PC$_{61}$BM than for **2**:PC$_{71}$BM, we assume that the smaller C$_{60}$-derivative can diffuse better.

The slightly better performance of OPV devices fabricated with **2**:P$_{71}$CBM than with **2**:P$_{61}$CBM can be attributed to the stronger absorbance in the whole spectral range of the PC$_{71}$BM.

Regardless of the processing conditions, the air-film surface of the films has a skin layer enriched with oligomer, possibly formed as result of the surface energy difference between the oligomer and the fullerene component. This layer seems to cause no impact in the OPV performance.

Conclusions

We have identified the morphological differences in the solar cell active layers of two A-D-A type structural isomers. Their dissimilar photovoltaic performance and reaction to SVA

treatment could be rationalized by their different chemical structures: Isomer **1** (hexyl chains at the outer positions of the thiophene rings) and isomer **2** (inner positions).

Although the inner positioned hexyl side chains of isomer **2** hinder the π-π stacking during the fast evaporation process of spin-coating, they also allow larger diffusive motion of the molecules during the process of solvent vapor annealing. This facilitates molecular rearrangement to achieve a thermodynamically more favorable nanomorphology. The reorganization process involves the formation of larger, separated D:A domains, and the segregation of fullerene towards the top of the film. Films fabricated with **2**:$PC_{71}BM$ yield a dramatic increase in PCE from 1.1 to 7.1% upon SVA. It can be expected that further improvement in device performance could be achieved through the use of solvent additives to better control the crystallization dynamics during film formation.

Experimental Section

Device fabrication

The oligomers **1** and **2** were synthesized as described before.[29] $PC_{61}BM$ ([6,6]-phenyl-C_{61}-butyric acid methyl ester, 99%) and $PC_{71}BM$ ([6,6]-phenyl-C_{71}-butyric acid methyl ester, 99%) were purchased from Solenne BV. The samples with **1**:$PC_{61}BM$ and **2**:$PC_{61}BM$ were prepared as described in the previous study.[29] For solar cells with **2**:$PC_{71}BM$ the absorber solution was prepared at ambient atmosphere with a total concentration of 20 mg mL^{-1} in $CHCl_3$ (EMSURE® purchased from Merck). After stirring at room temperature (r. t.) for at least 1 h, the solution was heated to 50 °C for 15 min and then cooled down to r. t. again. ITO-coated glass substrates from VisionTec (14 Ohm sq^{-1}) were structured and plasma etched (Diener electronic, Pico) with Argon for 120 s at 30W and a base pressure of 0.38 mbar. Then PEDOT:PSS (Clevios P VP.AI 4083 solution from Heraeus), which was diluted with deionized water in a 1:1 ratio was doctor bladed and ~10 nm thick layers were obtained. Afterwards, the substrates were spin-coated (Laurell CZ-650 series) with the absorber solution at 1000 rpm for 60 s leading to ~100 nm thick photoactive layers. The SVA was carried out by dropping 100 µl $CHCl_3$ around the as-cast BHJ layer and putting a petri dish over it in that way that the film is for 90 s in $CHCl_3$ atmosphere. Thin layers of LiF (3 Å) and Al (120 nm) were then evaporated at a pressure of 2×10^{-6} mbar in a Univex 450 from Leybold. The evaporation process has been optimized in our group earlier.[49] The photoactive area of the solar cells was between 0.11 and 0.14 cm^2.

Characterization

Current voltage analysis was carried out with a WACOM 2-lamp solar simulator (class AAA, AM 1.5G) and a Keithley 2400 current source measure unit. Short circuit current densities were verified by quantum efficiency measurements. The quantum efficiency measurements were performed using equipment from Optosolar. As light source we utilized a 100 W

xenon lamp and the filtered monochromatic light was monitored with a Si cell. A white bias light with 0.1 − 0.2 sun intensity was used. Film thickness was measured by using a high resolution field emission scanning electron microscope (Sirion XL30) from FEI.

Negative SIMS was performed by a Leybold SSM 200 system using 5 keV primary Ar^+-ions. The sputtered area was 3 × 3 mm^2.

GIWAXS: The studied samples were spin coated on glass substrates covered with a thin PEDOT:PSS layer forming absorber blends with a thickness of 70 nm (**1**:$PC_{61}BM$), 90 nm (**2**:$PC_{61}BM$), and 110 nm (**2**:$PC_{71}BM$), respectively. (Also samples on ITO instead of pure glass have been studied and no difference was found.) GIWAXS measurements were done at the Ångstromquelle Karlsruhe (ANKA), Germany, with 12 keV photon energy at the beamline MPI. The 2D frames were taken by an X-ray area detector (MarCCD) and the in plane scans were obtained with a point detector varying the incident angle from 0.10º (below the critical angle) to 0.14º (above the critical angle). All the profiles are given as a function of the magnitude of the scattering vector q (Fig. S4a in the ESI†).

Atomic force microscopy (AFM) and Kelvin probe force microscopy (KPFM): Measurements were performed under inert conditions on a Bruker Dimension ICON atomic force microscope equipped with a Nanoscope V controller. Imaging was carried out in tapping mode with platinum-iridium coated silicon cantilevers (SCM-PIT from Bruker). Measurements were performed on active layers spin coated on ITO glass with an intermediate PEDOT:PSS layer.

Photoluminescence (PL) spectroscopy: Thin films were excited at 532 nm with a solid state laser in continuous wave operation (MGL-III-532, Changchun New Industries) at an excitation power of 80 mW. The laser beam was expanded to a spot size of 6 mm in diameter in order to probe a rather large sample volume. Photoluminescence was fiber-coupled into a spectrograph (Acton Research SpectraPro 300i) and detected with an intensified CCD (Princeton Research, PiMax 512).

Acknowledgements

Notes and references

1   S.-H. Liao, H.-J. Jhuo, P.-N. Yeh, Y.-S. Cheng, Y.-L. Li, Y.-H. Lee, S. Sharma and S.-A. Chen, *Sci. Rep.*, 2014, **4**, 6813.
2   J.-D. Chen, C. Cui, Y.-Q. Li, L. Zhou, Q.-D. Ou, C. Li, Y. Li and J.-X. Tang, *Adv. Mater.*, 2015, **27**, 1035.

3   B. Kan, M. Li, Q. Zhang, F. Liu, X. Wan, Y. Wang, W. Ni, G. Long, X. Yang, H. Feng, Y. Zuo, M. Zhang, F. Huang, Y. Cao, T. P. Russell and Y. Chen, *J. Am. Chem. Soc.*, 2015, **137**, 3886.
4   H. Zhou, Y. Zhang, C.-K. Mai, S. D. Collins, G. C. Bazan, T.-Q. Nguyen and A. J. Heeger, *Adv. Mater.*, 2015, **27**, 1767.
5   A. R. bin M. Yusoff, D. Kim, H. P. Kim, F. K. Shneider, W. J. da Silva and J. Jang, *Energy Env. Sci.*, 2015, **8**, 303.
6   J. Peet, J. Y. Kim, N. E. Coates, W. L. Ma, D. Moses, A. J. Heeger and G. C. Bazan, *Nat. Mater.,* 2007, **6**, 497.
7   K. R. Graham, P. M. Wieruszewski, R. Stalder, M. J. Hartel, J. Mei, F. So and J. R. Reynolds, *Adv. Funct. Mater.,* 2012, **22**, 4801.
8   E. Verploegen, R. Mondal, C. J. Bettinger, S. Sok, M. F. Toney and Z. Bao, *Adv. Funct. Mater.,* 2010, **20**, 3519.
9   B. Gholamkhass and P. Servati, *Org. Electron.*, 2013, **14**, 2278.
10 H. Tang, G. Lu, L. Li, J. Li, Y. Wang and X. Yang, *J. Mater. Chem.,* 2010, **20**, 683.
11 G. Wei, S. Wang, K. Sun, M. E. Thompson and S. R. Forrest, *Adv. Energy Mater.,* 2011, **1**, 184.
12 M. Li, F. Liu, X. Wan, W. Ni, B. Kan, H. Feng,Q. Zhang, X. Yang, Y. Wang, Y. Zhang, Y. Shen, T. P. Russell and Y. Chen, *Adv. Mater.*, 2015, DOI: 10.1002/adma.201502645.
13 A. Mishra and P. Bäuerle, *Angew. Chem. Int. Ed.,* 2012, **51**, 2020.
14 Y. Chen, X. Wan and G. Long, *Acc. Chem. Res*., 2013, **46**, 2645.
15 X. Xiao, G. Wei, S. Wang, J. D. Zimmerman, C. K. Renshaw, M. E. Thompson and S. R. Forrest, *Adv. Mater.*, 2012, **24**, 1956.
16 H. Bürckstümmer, E. V. Tulyakova, M. Deppisch, M. R. Lenze, N. M. Kronenberg, M. Gsänger, M. Stolte, K. Meerholz and F. Würthner, *Angew. Chem. Int. Ed*., 2011, **50**, 11628.
17 B. Yin, L. Yang, Y. Liu, Y. Chen, Q. Qi, F. Zhang and S. Yin, *Appl. Phys. Lett*., 2010, **97**, 023303–1.
18 G. Long, X. Wan, B. Kan, Y. Liu, G. He, Z. Li, Y. Zhang, Y. Zhang, Q. Zhang, M. Zhang and Y. Chen, *Adv. Energy Mater*., 2013, **3**, 639.
19 Y. Liu, X. Wan, F. Wang, J. Zhou, G. Long, J. Tian, J. You, Y. Yang and Y. Chen, *Adv. Energy Mater*., 2011, **1**, 771.
20 Y. Liu, Y. (M.) Yang, C.-C. Chen, Q. Chen, L. Dou, Z. Hong, G. Li and Y. Yang, *Adv. Mater.,* 2013, **25**, 4657.
21 B. Walker, C. Kim and T.-Q. Nguyen, *Chem. Mater*., 2011, **23**, 470.
22 J. Zhou, X. Wan, Y. Liu, G. Long, F. Wang, Z. Li, Y. Zuo, C. Li and Y. Chen, *Chem. Mater*., 2011, **23**, 4666.
23 Y. Sun, G. C. Welch, W. L. Leong, C. J. Takacs, G. C. Bazan and A. J. Heeger, *Nat. Mater.,* 2011, **11**, 44.
24 T. S. van der Poll, J. A. Love, T.-Q. Nguyen and G. C. Bazan, *Adv. Mater.,* 2012, **24**, 3646.
25 V. Gupta, A. K. K. Kyaw, D. H. Wang, S. Chand, G. C. Bazan and A. J. Heeger, *Sci. Rep*. 2013, **3**, 1965.
26 A. K. K. Kyaw, D. H. Wang, D. Wynands, J. Zhang, T.-Q. Nguyen, G. C. Bazan and A. J. Heeger, *Nano Lett*., 2013, **13**, 3796.
27 D. H. Wang, A. K. K. Kyaw, V. Gupta, G. C. Bazan and A. J. Heeger, *Adv. Energy Mater*., 2013, **3**, 1161.
28 M. Weidelener, C. D. Wessendorf, J. Hanisch, E. Ahlswede, G. Götz, M. Lindén, G. Schulz, E. Mena-Osteritz, A. Mishra and P. Bäuerle, *Chem. Commun*., 2013, **49**, 10865.
29 C. D. Wessendorf, G. L. Schulz, A. Mishra, P. Kar, I. Ata, M. Weidelener, M. Urdanpilleta, J. Hanisch, E. Mena-Osteritz, M. Lindén, E. Ahlswede and P. Bäuerle, *Adv. Energy Mater*., 2014, **4**, 1400266.
30 F. Liu, Y. Gu, X. Shen, S. Ferdous, H.-W. Wang and T. P. Russell, *Prog. Polym. Sci.,* 2013, **38**, 1990.
31 M. R. Hammond, R. J. Kline, A. A. Herzing, L. J. Richter, D. S. Germack, H.-W. Ro, C. L. Soles, D. A. Fischer, T. Xu, L. Yu, M. F. Toney and D. M. DeLongchamp, *ACS Nano,* 2011, **5**, 8248.

32 X. Yang, J. K. J. van Duren, M. T. Rispens, J. C. Hummelen, R. A. J. Janssen, M. A. J. Michels and J. Loos, *Adv. Mater.,* 2004, **16**, 802.
33 B. Schmidt-Hansberg, M. F. G. Klein, M. Sanyal, F. Buss, G. Q. G. de Medeiros, C. Munuera, A. Vorobiev, A. Colsmann, P. Scharfer, U. Lemmer, E. Barrena and W. Schabel, *Macromolecules,* 2012, **45**, 7948.
34 J.-L. Bredas, D. Beljonne, V. Coropceanu and J. Cornil, *Chem. Rev.* 2004, **104**, 4971.
35 L. A. Perez, K. W. Chou, J. A. Love, T. S. van der Poll, D.-M. Smilgies, T.-Q.Nguyen, E. J. Kramer, A. Amassian and G. C. Bazan, *Adv. Mater.* 2013, **25**, 6380.
36 Q. Zhang, B. Kan, F. Liu, G. Long, X. Wan, X. Chen, Y. Zuo, W. Ni, H. Zhang, M. Li, Z. Hu, F. Huang, Y. Cao, Z. Liang, M. Zhang, T. P. Russell and Y. Chen, Nat. Photon., 2015, **9**, 35.
37 M. He, M. Wang, C. Lin and Z. Lin, *Nanoscale*, 2014, **6**, 3984.
38 N. D. Treat and M. L. Chabinyc, *Annu. Rev. Phys. Chem.,* 2014, **65**, 59.
39 A. J. Heeger, *Adv. Mater.,* 2014, **26**, 10.
40 S. Sadewasser, T. Glatzel, M. Rusu, A. Jäger-Waldau and M. C. Lux-Steiner, *Appl. Phys. Lett.,* 2002, **80**, 2979.
41 C.-S. Jiang, H. R. Moutinho, D. J. Friedman, J. F. Geisz and M. M. Al-Jassim, *J. Appl. Phys.,* 2003, **93**, 10035.
42 C. Barth and C. R. Henry, *Appl. Phys. Lett.,* 2006, **89**, 252119.
43 K. Maturová, M. Kemerink, M. M. Wienk, D. S. H. Charrier and R. A. J. Janssen, *Adv. Funct. Mater.,* 2009, **19**, 1379.
44 V. Palermo, G. Ridolfi, A. M. Talarico, L. Favaretto, G. Barbarella, N. Camaioni and P. Samorì, *Adv. Funct. Mater.,* 2007, **17**, 472.
45 M. Chiesa, L. Bürgi, J.-S. Kim, R. Shikler, R. H. Friend, H. Sirringhaus, *Nano Lett.,* 2005, **5**, 559.
46 H. Hoppe, T. Glatzel, M. Niggemann, A. Hinsch, M. C. Lux-Steiner and N. S. Sariciftci, *Nano Lett.,* 2005, **5**, 269.
47 M. Campoy-Quiles, T. Ferenczi, T. Agostinelli, P. G. Etchegoin, Y. Kim, T. D. Anthopoulos, P. N. Stavrinou, D. D. C. Bradley and J. Nelson, *Nat. Mater.,* 2008, **7**, 158.
48 Z. Xu, L. M. Chen, G. W. Yang, C. H. Huang, J. H. Hou, Y. Wu, G. Li, C. S. Hsu and Y. Yang, *Adv. Funct. Mater.,* 2009, **19**, 1227.
49 E. Ahlswede, J. Hanisch and M. Powalla, *Appl. Phys. Lett*., 2007, **90**, 063513.

Journal of Materials Chemistry A Accepted Manuscript

i) oligomer-enriched surface
ii) sub-surface region with decreased concentration of oligomer
iii) a slightly oligomer-enriched region up to the bottom interface with more or less constant signals

Solvent vapor annealing (SVA) can strongly influence the morphology of oligomer:fullerene – based organic solar cells: while for oligomer **1** with alkyl chains at the "outer" positions only crystallinity and domain size are increased, for oligomer **2** with alkyl chains at the more sterically hindered "inner" positions additionally a vertical gradient is formed after SVA.